

# Single-View Holographic Volumetric 3D Printing with Coupled Differentiable Wave-Optical and Photochemical Optimization

FELIX WECHSLER, École Polytechnique Fédérale de Lausanne (EPFL), Switzerland

RICCARDO RIZZO, École Polytechnique Fédérale de Lausanne (EPFL), Switzerland

CHRISTOPHE MOSER, École Polytechnique Fédérale de Lausanne (EPFL), Switzerland

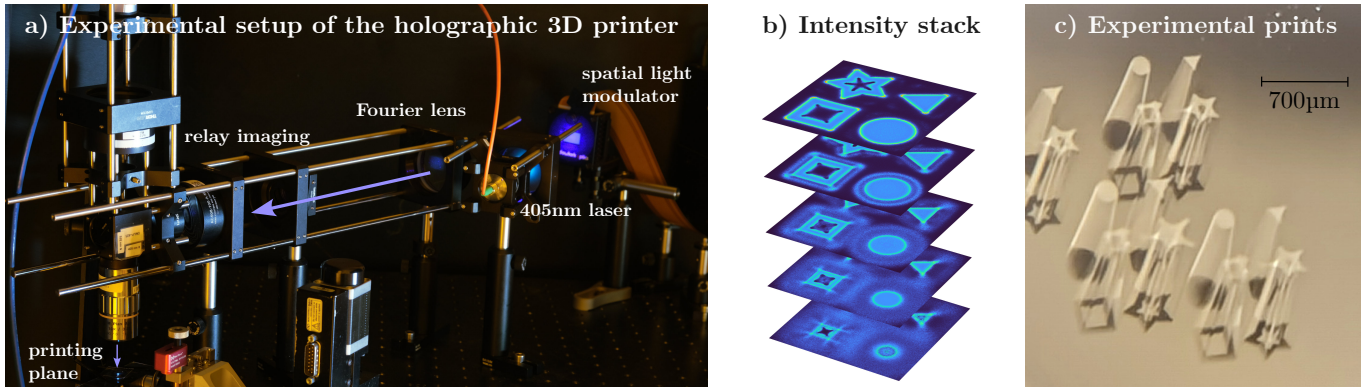


Fig. 1. **a)** SHVAM overview: a 405 nm laser is phase-modulated by a spatial light modulator (SLM) and relayed through a Fourier holography optical system into a photosensitive resin, enabling mechanically static, single-axis volumetric exposure. **b)** Volumetric printing is posed as a coupled inverse problem: we optimize a time-multiplexed sequence of phase-only holograms so that the *accumulated* 3D dose matches a target, while explicitly accounting for inhibition and diffusion in a differentiable photochemical model to pre-compensate chemical blur. **c)** Representative prints demonstrating rapid fabrication and improved fidelity from chemistry-aware optimization; each group of elements is fabricated in 8 s.

Volumetric additive manufacturing promises near-instantaneous fabrication of 3D objects, yet achieving high fidelity at the micro-scale remains challenging due to the complex interplay between optical diffraction and chemical effects. We present *Single-View Holographic Volumetric Additive Manufacturing* (SHVAM), a mechanically static system that shapes volumetric dose distributions using time-multiplexed, phase-only holograms projected from a single optical axis. To achieve high resolution with SHVAM, we formulate hologram synthesis as a coupled inverse problem, integrating a differentiable wave-optical forward model with a simplified photochemical model that explicitly captures inhibitor diffusion and non-linear dose response. Optimizing hologram sequences under these coupled constraints allows us to pre-compensate for chemical blur, yielding higher print fidelity than optical-only optimization. We demonstrate the efficacy of SHVAM by fabricating simple 2D and 3D structures with lateral feature sizes of approximately 10 μm within a 0.8 mm × 0.8 mm × 3 mm volume in seconds.

Additional Key Words and Phrases: Holography, 3D printing, volumetric additive manufacturing, wave optics, differentiable optics

## 1 INTRODUCTION

To overcome fundamental speed limitations of layer-by-layer printing while retaining geometric freedom, Volumetric Additive Manufacturing (VAM) was introduced to fabricate entire objects in a single exposure process [Shusteff et al. 2017]. In Tomographic Volumetric Additive Manufacturing (TVAM), a 3D volume is formed

Authors' addresses: Felix Wechsler, École Polytechnique Fédérale de Lausanne (EPFL), Switzerland, shvam@felixwechsler.science; Riccardo Rizzo, École Polytechnique Fédérale de Lausanne (EPFL), Switzerland, riccardo.rizzo@epfl.ch; Christophe Moser, École Polytechnique Fédérale de Lausanne (EPFL), Switzerland, christophe.moser@epfl.ch.

through tomographic back-projection of 2D patterns while a resin vial rotates [Kelly et al. 2019; Bernal et al. 2019; Loterie et al. 2020].

A key challenge across these lithographic techniques is that print outcomes depend not only on optics but also on resin chemistry. Accurate chemistry modeling is essential to predict reaction kinetics and diffusion processes that govern polymerization and final material properties [Weisgraber et al. 2023]. In particular, diffusion of chemical inhibitors such as oxygen or TEMPO (2,2,6,6-tetramethylpiperidine 1-oxyl) can produce visible defects if not accounted for [Orth et al. 2023; Zhang et al. 2025]. Data-driven approaches can learn systematic correction of prints, as demonstrated for Two-Photon polymerization [Zheng et al. 2023].

In this work, we focus on volumetric printing driven by computer-generated holography (CGH), which enables shaping optical fields by phase modulation. A common implementation uses a Spatial Light Modulator (SLM) to modulate a coherent beam in Fourier space, with a lens mapping phase modulation to intensity in the target plane; off-axis carrier ramps are often used to separate the reconstruction from the zero-order spot [Efron 1994; Goodman 2017]. Recent advances in CGH increasingly rely on differentiable wave propagation models to improve fidelity and compensate for system aberrations [Peng et al. 2020; Choi et al. 2021].

We introduce a mechanically static, single-view volumetric printing setup that uses Fourier-domain holographic projections to fabricate 3D objects (see Figure 2). We call our approach *Single-View Holographic Volumetric Additive Manufacturing* (SHVAM). SHVAM optimizes a time-multiplexed sequence of phase-only holograms

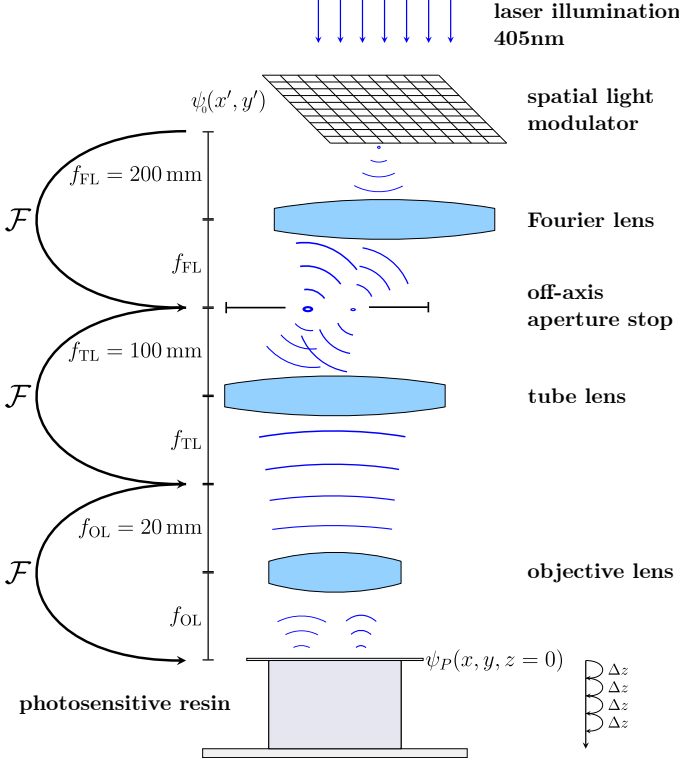


Fig. 2. Schematic of the SHVAM printer. A coherent beam is phase-modulated by a spatial light modulator (SLM) and Fourier-transformed by a lens. The strong zero-order (unmodulated) component arising from the pixelated SLM is suppressed using an off-axis spatial filter. A relay imaging system (tube lens and microscope objective) then re-imagines the filtered field into the resin at the printing plane ( $z = 0$ ), from which the 3D field distribution is computed via angular-spectrum wave propagation.

such that the accumulated 3D energy deposition in a photosensitive resin matches a target dose distribution. In our prototype, we project holograms using a coherent 405 nm laser and a phase-only SLM imaged through a microscope objective. This enables faster VAM printing, as it eliminates mechanical rotation and relies solely on the laser power and projection refresh rate.

Producing complex volumetric dose distributions from a single optical axis requires solving a constrained inverse problem. We therefore couple phase optimization with a wave-optical forward model based on angular-spectrum propagation. To improve fidelity for fine features, we further incorporate a photochemical model directly into the objective, accounting for radical generation, inhibitor concentration, and inhibitor diffusion during exposure. We validate the proposed model and optimization by fabricating a range of 2D and 3D structures in seconds and by comparing predictions against experimental outcomes.

Our contributions are:

- A single-view, phase-only hologram synthesis method for volumetric 3D printing based on a wave-optical forward model.

- A differentiable photochemical model for volumetric 3D printing that explicitly captures inhibitor diffusion and non-linear dose response. While demonstrated here for holographic printing, this formulation is applicable to many light-based volumetric printers (e.g., TVAM).
- Experimental validation on 2D and 3D prints, demonstrating the impact of the photochemical model on print fidelity.

We discuss current limitations in printable volume and fidelity, and outline directions to scale SHVAM through improved calibration, optics, and resin characterization. By adopting a static single-view architecture instead of mechanical rotation (as in TVAM), we explicitly trade axial resolution for mechanical simplicity and fabrication speed. While the axial resolution remains limited by the low numerical aperture (NA) required to maintain a wide field of view, this configuration enables the rapid generation of micro-structures without moving parts.

Our reference implementation can be found at: *Code will be released upon acceptance*

## 2 BACKGROUND AND RELATED WORK

**Additive Manufacturing.** Additive manufacturing has evolved from rapid prototyping into a family of processes capable of industrial-scale and micro-scale fabrication. Classic layer-by-layer approaches include extrusion-based methods such as Fused Deposition Modeling [Crump 1992] and vat photopolymerization techniques such as Stereolithography (SLA) [Hull 1986; Kodama 1981] and Digital Light Processing [Hornbeck 1997]. A major step toward faster photopolymer printing was Continuous Liquid Interface Production, which uses an oxygen-permeable window to form a *dead zone* that enables continuous fabrication [Tumbleston et al. 2015]. In parallel, the demand for high-resolution microfabrication led to micro-SLA [Ikuta and Hirowatari 1993] and, for sub-diffraction precision, Two-Photon Polymerization (2PP) [Maruo et al. 1997]. While 2PP offers exceptional resolution, volumetric throughput is typically limited by serial point scanning; holographic multiplexing can increase throughput by generating multiple foci simultaneously [Zhang et al. 2024], and more complex holographic 2PP has been theoretically considered for high-power single laser pulses [Somers et al. 2024].

**Volumetric Additive Manufacturing (VAM).** SHVAM is most closely connected to prior work on volumetric additive manufacturing. Early volumetric fabrication demonstrations (not yet referred to as VAM) used holographic interference of coherent beams to create periodic structures [Campbell et al. 2000]. Later, Shusteff et al. [2017] introduced a VAM system using three intersecting (but not coherently interfering) beams. This formulation admits efficient fabrication but restricts printable geometries because the light transport is modeled as a small set of collimated rays, limiting achievable shapes to combinations compatible with the available beam directions.

**Tomographic Volumetric Additive Manufacturing (TVAM).** Tomographic Volumetric Additive Manufacturing (TVAM) generalizes VAM by projecting a sequence of tomographic light patterns into a rotating vial of photosensitive resin [Kelly et al. 2019; Loterie et al. 2020]. In these systems, projected energy is attenuated according to Beer–Lambert absorption [Kelly et al. 2019] and initiates free-radical

polymerization. TVAM relies on a nonlinear threshold response: projected patterns are optimized so that target regions exceed the polymerization threshold while void regions remain below it [Kelly et al. 2019; Rackson et al. 2021; Bhattacharya et al. 2021]. Inverse rendering techniques that explicitly model light transport enable improved fidelity across optical scenarios [Nicolet et al. 2024]. TVAM is also particularly attractive for bioprinting [Bernal et al. 2019] and overprinting onto existing absorbing, scattering, refracting or reflective structures [Wechsler et al. 2025].

*Chemical effects in VAM.* A practical complication is inhibition. Once radicals are generated, they can be quenched by inhibitors such as dissolved oxygen; polymerization initiation and propagation become effective only after local inhibitor depletion [Zhang et al. 2025]. This depletion can introduce spatiotemporal dynamics, including diffusion-driven blur that affects print fidelity. Orth et al. [2023] modeled inhibitor-related artifacts by modifying the distributed dose with a convolution-like operation, which captures some qualitative effects but does not explicitly represent chemical diffusion in the resin. Beyond oxygen, TEMPO has been explored as an additional inhibitor [Toombs et al. 2022; Thijssen et al. 2024]; improved fidelity is often attributed to reduced diffusion compared to oxygen, though quantitative integration of TEMPO dynamics into pattern generation remains limited.

*Wave-optical TVAM projections.* On the optical side, TVAM patterns are most commonly projected via amplitude modulation, but phase modulation has also been demonstrated [Álvarez Castaño et al. 2025]. That work, however, uses a ray-optical description and therefore does not constitute a fully wave-optical holographic model of light transport. Wechsler et al. [2024] introduced a theoretical wave-optical light transport formulation for TVAM, which is, in principle, compatible with phase-modulated systems.

*Holographic VAM.* Related wave-optical optimization schemes for holographic printers have been presented by Li et al. [2024] and Moser et al. [[n. d.]]; Li et al. [2024] additionally modeled an inhibition beam, and later provided simple experimental demonstrations with two orthogonal projections [Li 2024]. The use of multiple views (compared to one view in this work) was motivated by the limited spatial-frequency coverage of a single projection objective (see Appendix G). Very recently, a static single-view phase-mask-based holographic printer was proposed [Lin et al. 2026]. While closely related in basic principles to this work, it relies on a single, non-reconfigurable phase element, producing one coherent field realization in the volume and thus remaining constrained by monochromatic wave propagation (the Helmholtz equation). In contrast, SHVAM uses time-multiplexed phase patterns whose dose accumulation is effectively incoherent (when a large amount of patterns is used), enabling volumetric dose distributions that are not attainable from any single coherent propagation; see Appendix E for discussion. Further, their work does not model any chemical effects quantitatively and will result in limited resolutions as we demonstrate in this work.

### 3 METHODOLOGY

The core of SHVAM’s modeling is a wave-optical simulation that describes how a phase-modulated coherent pattern produces a 3D intensity distribution. The accumulated polymerization dose in the photosensitive resin results from time-integrating the intensities from a set of such patterns. However, as shown in this work, additionally modeling the photochemical kinetics of the resin is key to achieving high-resolution prints. We therefore introduce explicit (albeit simplified) modeling of inhibitors and their chemically induced diffusion.

#### 3.1 Optical model

The optical setup is shown in Figure 2. We use a phase-modulating spatial light modulator (SLM) to imprint a phase pattern  $\varphi_j$  onto an incident coherent field  $\psi_0(x', y')$ . The modulated field is relayed through a standard Fourier holography configuration: a Fourier lens of focal length  $f_{FL}$  performs an optical Fourier transform, and an off-axis aperture selects a single diffraction order to suppress the strong on-axis (zero-order) component caused by unmodulated light from the SLM [Efron 1994]. The selected field is then reimaged into the resin volume using a tube lens and a microscope objective. The overall demagnification from the aperture plane to the printing plane is

$$M = \frac{f_{OL}}{f_{TL}}, \quad (1)$$

where  $f_{OL}$  and  $f_{TL}$  denote the focal lengths of the objective and tube lens, respectively.

Let  $\Delta x$  be the SLM pixel pitch and  $N$  the number of SLM pixels along one dimension. Under the usual Fourier scaling for a lens-based Fourier transform [Goodman 2017], the effective sampling in the aperture (Fourier) plane is

$$\Delta x_A = \frac{\lambda f_{FL}}{N \Delta x}. \quad (2)$$

After demagnification into the printing plane, the effective sampling becomes

$$\Delta x_P = \frac{\lambda f_{FL} f_{OL}}{N \Delta x f_{TL}}, \quad (3)$$

where  $\lambda = 405$  nm is the vacuum wavelength.

Given a displayed phase pattern  $\varphi_j(x', y')$  on the SLM, the complex field at the printing plane ( $z = 0$ ) can be written (up to a constant scaling factor) as

$$\psi_{P,j}(x, y, 0) \sim \mathcal{F}[\psi_0(x', y') \exp(i \varphi_j(x', y'))](x, y), \quad (4)$$

where  $(x', y')$  are continuous coordinates on the SLM and  $(x, y)$  denote continuous coordinates in the printing plane.

To model propagation from the printing plane into the resin volume, we use band-limited angular spectrum propagation [Matushima and Shimobaba 2009; Wechsler et al. 2024]:

$$\psi_{P,j}(x, y, z) = \mathcal{F}^{-1}[H_{AS}(z) \mathcal{F}[\psi_{P,j}(x, y, 0)]] = \mathcal{A}_z[\psi_{P,j}(x, y, 0)], \quad (5)$$

with transfer function

$$H_{AS}(z) = \exp\left(i 2\pi n z \sqrt{\frac{1}{\lambda^2} - f_x^2 - f_y^2}\right), \quad (6)$$

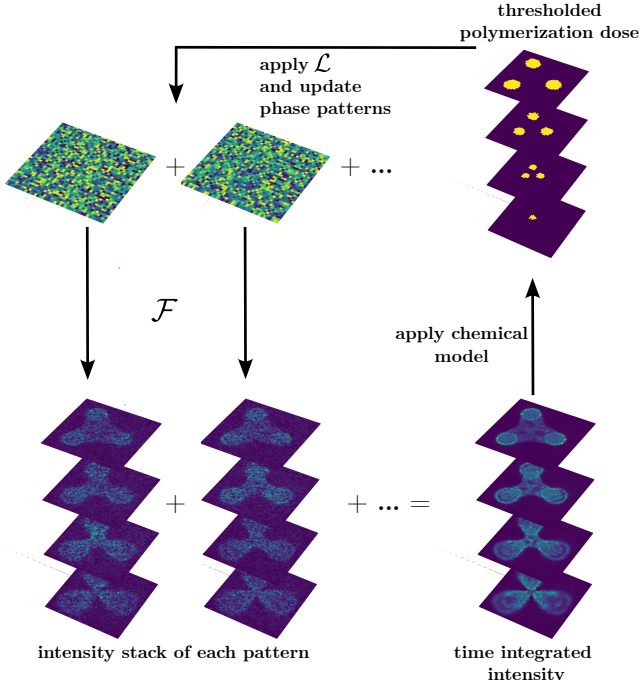


Fig. 3. Visual description of the optimization process. A fixed number of phase patterns is projected into the resin which results in the intensity summation of those patterns. Their sum results in a time integrated intensity. After applying the chemical model we obtain a binary solidified print. Evaluating this print and the chemical concentrations with our loss function allows to update the phase patterns via gradient-descent based optimization.

where  $n$  is the refractive index of the resin and  $(f_x, f_y)$  are spatial frequencies.

In the context of printing, the resin integrates optical intensity over time, and light is attenuated along depth according to Beer-Lambert absorption. We therefore model the accumulated absorbed dose  $D(x, y, z)$  as

$$D(x, y, z) \sim T_{\text{exp}} \mu \exp(-\mu z) \sum_{j=1}^K |\mathcal{A}_z[\psi_{P,j}(x, y, 0)]|^2, \quad (7)$$

where  $\mu$  is the absorption coefficient of the resin (primarily determined by photoinitiator concentration),  $T_{\text{exp}}$  is the total exposure time,  $K$  is the number of time-multiplexed phase patterns, and  $\psi_{P,j}$  denotes the printing-plane field produced by phase pattern  $\varphi_j$ .

We sum over patterns because each hologram is displayed for a short interval  $\Delta t \ll T_{\text{exp}}$  and the resin effectively accumulates the *incoherent* sum of intensities. Time multiplexing provides two practical benefits: (i) it reduces coherent speckle artifacts through temporal averaging, and (ii) it increases the expressiveness of attainable 3D dose distributions compared to a single coherent field realization (see Appendix E). Equation 7 is fully differentiable and can be evaluated with FFT-based propagation at a computational cost of approximately  $\mathcal{O}(K \cdot N_z \cdot N^2 \log N)$  for a cubic  $N \times N \times N_z$  voxel volume.

### 3.2 Chemical model

The second component of our forward model is a simplified description of the underlying photochemistry. Given the wave-optical intensity field in the resin volume, the chemical model predicts a polymerization field and thus a final (thresholded) print outcome, as illustrated in Figure 3.

Although we apply this model to a single-view holographic setup, the underlying reaction-diffusion kinetics depend solely on the accumulated 3D light intensity distribution and material parameters. Consequently, this differentiable chemical module is agnostic to the optical delivery method and can be readily adapted to improve fidelity in other volumetric approaches.

In principle, the full reaction network governing volumetric additive manufacturing (VAM) can be modeled in detail [Weisgraber et al. 2023]. However, comprehensive kinetic models require characterization of a large set of rate constants and material parameters and are typically used as forward simulators rather than as differentiable components inside an inverse-design loop. To avoid an extensive parameter-identification procedure while still capturing the dominant resolution-limiting mechanisms, we adopt a simplified model that retains the key effects of inhibition and inhibitor diffusion.

In TVAM and related approaches, polymerization is approximated by a threshold model: a light pattern is projected for a prescribed duration, and voxels are assumed to solidify once the absorbed dose exceeds a fixed threshold. While convenient, this description is not sufficiently accurate for predicting (and compensating) inhibition-driven effects.

At the onset of exposure, incident light is absorbed by the photoinitiator (PI), generating reactive radicals that can initiate polymerization. In practice, inhibition reactions due to dissolved oxygen and/or added inhibitors such as TEMPO are orders of magnitude faster than propagation reactions [Weisgraber et al. 2023; Zhang et al. 2025]. Consequently, as long as the local inhibitor concentration is non-zero, radical quenching dominates and polymerization is strongly suppressed. Once inhibitors are locally depleted, concentration gradients form and induce diffusive transport, which couples the chemistry across space.

Our resin contains two inhibitors: oxygen and TEMPO. The latter is comparatively large and diffuses slowly, whereas oxygen diffuses significantly faster. Starting from the full model in [Weisgraber et al. 2023], we apply the following assumptions to obtain a computationally tractable reduced model:

- The monomer concentration  $c[M]$  is assumed constant over the exposure time.
- Radicals that are not inhibited contribute to an accumulated polymerization field  $c[P^*]$ .
- The temperature is constant.
- Polymerization is local (i.e., we neglect spatial growth and transport of polymer chains).
- Diffusion of inhibitors ( $O_2$ , TEMPO) is modeled explicitly; diffusion of PI and radicals is neglected due to their comparatively low mobility (consistent with the size dependence of diffusion described by the Stokes-Einstein relation).

Note that PI depletion in principle occurs during illumination; including it would require dynamically updating local absorption and increases computational cost. In our reduced model, we therefore treat PI as effectively constant and absorb its contribution into an effective radical-generation term. Likewise, we do not explicitly model chain growth and termination kinetics; instead, their net effect is captured by an effective propagation term contributing to  $c[P^*]$ .

Under these assumptions we can analyze the kinetic rate equations:

$$\begin{aligned} \frac{\partial c[R]}{\partial t} &= 2k_I I c[PI] - k_p c[M] c[R] - k_{O_2} c[O_2] c[R] \\ &\quad - k_{TEMPO} c[TEMPO] c[R] \\ \frac{\partial c[O_2]}{\partial t} &= \nabla^2 \cdot (D_{O_2} c[O_2]) - k_{O_2} c[O_2] c[R] \\ \frac{\partial c[TEMPO]}{\partial t} &= \nabla^2 \cdot (D_{TEMPO} c[TEMPO]) - k_{TEMPO} c[TEMPO] c[R] \\ \frac{\partial c[P^*]}{\partial t} &= k_p c[M] c[R]. \end{aligned}$$

Here,  $I$  denotes the local light intensity,  $k_I$  is the rate constant for light-triggered radical generation,  $k_p$  is an effective propagation rate constant,  $k_{O_2}$  and  $k_{TEMPO}$  govern inhibition, and  $D_{O_2}$ ,  $D_{TEMPO}$  are diffusion coefficients.

For numerical efficiency in inverse design, we exploit the separation of timescales  $k_{O_2} > k_{TEMPO} \gg k_p$ , which implies that newly generated radicals are preferentially quenched by oxygen, then by TEMPO, and only the remaining radicals contribute substantially to polymerization. We therefore do not explicitly integrate the reaction-diffusion system since it would require precise knowledge of the absolute values of photochemical constants. Instead, we use an operator-splitting surrogate: at each time step we (i) generate radicals proportional to the local intensity, (ii) quench radicals by available inhibitors (oxygen, then TEMPO), (iii) accumulate polymerization from the remaining radicals, and (iv) diffuse inhibitor concentrations.

Finally, the inhibitor diffusion step can be implemented efficiently using the Green's function of the diffusion equation. For constant diffusion coefficient  $D$ , a diffusion step of duration  $\Delta T$  corresponds to convolution with a Gaussian kernel,

$$K^{\Delta T}(x, y, z) = \frac{1}{(4\pi D \Delta T)^{3/2}} \exp\left(-\frac{x^2 + y^2 + z^2}{4D\Delta T}\right), \quad (8)$$

which we evaluate numerically via FFT-based convolutions [Orth et al. 2023]. We do not apply padding (usually applied to avoid circular convolution artifacts) as our kernel size is small and we have sufficient padding around the target. Overall, the reduced chemical modeling used inside our inverse-design loop is summarized in Algorithm 1. To connect the time-discretized chemistry surrogate to the experiment, we interpret one chemical timestep  $\Delta T$  as one *pattern cycle*: the duration required to display the full set of  $K$  optimized holograms once on the SLM (each for  $\Delta t$ , with  $\Delta T = K \Delta t$ ). During a print, this cycle is repeated  $N_{rep}$  times, so that the total exposure time is  $T_{exp} = N_{rep} \Delta T$  (in our experiments,  $N_{rep} \approx 15-20$ ). Within each cycle, we model radical generation using the intensity produced by the  $K$  holograms (Eq. 7), while inhibitor diffusion and

---

**Algorithm 1** Reduced photochemistry surrogate with inhibition and diffusion (used inside inverse design)

---

```

1: Input: target design, time step  $\Delta T$ , total exposure time  $T_{exp}$ , diffusion kernels  $K_{O_2}^{\Delta T}, K_{TEMPO}^{\Delta T}$ , scaling parameter  $\alpha$ 
2: Output: Phase patterns  $\{\varphi_j\}_{j=1}^K$ 
3:  $N_T \leftarrow T_{exp}/\Delta T$ 

4: for optimization iteration  $m = 1, 2, \dots, M$  do
5:    $c[P^*] \leftarrow 0$ 
6:    $c[O_2] \leftarrow c[O_2]_0$ 
7:    $c[TEMPO] \leftarrow c[TEMPO]_0$ 
8:   Compute dose field  $D(\mathbf{r})$  from  $\{\varphi_j\}$  (Eq. 7)

9:   for  $n = 1, 2, \dots, N_T$  do
10:    Radical generation:  $c[R] \leftarrow \alpha D/N_T$ 
11:    Quenching oxygen:
12:       $q_{O_2} \leftarrow \min(c[R], c[O_2])$ 
13:       $c[R] \leftarrow c[R] - q_{O_2}$ 
14:       $c[O_2] \leftarrow c[O_2] - q_{O_2}$ 
15:    Quenching TEMPO:
16:       $q_{TEMPO} \leftarrow \min(c[R], c[TEMPO])$ 
17:       $c[R] \leftarrow c[R] - q_{TEMPO}$ 
18:       $c[TEMPO] \leftarrow c[TEMPO] - q_{TEMPO}$ 
19:    Polymerization:  $c[P^*] \leftarrow c[P^*] + c[R]$ 
20:    # * indicates convolution
21:    Diffusion:  $c[O_2] \leftarrow c[O_2] * K_{O_2}^{\Delta T}$ 
22:     $c[TEMPO] \leftarrow c[TEMPO] * K_{TEMPO}^{\Delta T}$ 
23:   end for
24:   Compute loss  $\mathcal{L}(c[P^*], c[O_2], c[TEMPO])$  (Eq. 9)
25:   Update  $\{\varphi_j\}$  using L-BFGS
26: end for

```

---

depletion are updated once per cycle via the chemistry loop. Despite the strong simplifications of this approach, we show in section 4 that incorporating inhibitor diffusion inside the inverse-design loop yields consistent practical improvements in print fidelity.

### 3.3 Inverse modeling with chemically-informed loss function

To compute a set of holographic projection patterns, we solve a differentiable inverse problem over the SLM phase patterns  $\{\varphi_j\}_{j=1}^K$ . We use a gradient-based optimizer (L-BFGS [Liu and Nocedal 1989]) and backpropagate through the coupled forward model consisting of (i) wave-optical propagation and time-multiplexed intensity accumulation (Eq. 7) and (ii) the reduced photochemistry surrogate (Algorithm 1). As in other VAM approaches, the goal is to trigger sufficient polymerization in object regions while suppressing polymerization in void regions.

Let  $\Omega_{obj}$  denote the set of object voxels and  $\Omega_{void}$  the set of void voxels. The chemical forward model outputs the accumulated polymerization field  $c[P^*](\mathbf{r})$  as well as inhibitor fields  $c[O_2](\mathbf{r})$  and  $c[TEMPO](\mathbf{r})$  at the end of exposure. We define a loss that (i) enforces a target polymerization range in object voxels, (ii) penalizes inhibitor remaining inside the object (encouraging depletion where

polymerization should occur), (iii) suppresses polymerization in void voxels, and (iv) enforces that void regions retain a minimum amount of inhibitor, which empirically mitigates unintended curing due to inhibition loss.

We use  $\text{ReLU}(x) = \max(0, x)$  and define the loss:

$$\begin{aligned} \mathcal{L} = & \sum_{v \in \Omega_{\text{obj}}} |\text{ReLU}(T_P - c[\text{P}^*]_v)|^2 + |\text{ReLU}(c[\text{P}^*]_v - T_{\text{OP}})|^2 \\ & + \sum_{v \in \Omega_{\text{obj}}} (|c[\text{O}_2]_v|^2 + |c[\text{TEMPO}]_v|^2) \\ & + \sum_{v \in \Omega_{\text{void}}} (c[\text{P}^*]_v)^2 \\ & + \sum_{v \in \Omega_{\text{void}}} |\text{ReLU}(T_I - c[\text{O}_2]_v - c[\text{TEMPO}]_v)|^2. \end{aligned} \quad (9)$$

Here,  $T_P$  is the minimum polymerization level required for solidification (we use  $T_P = 0.1$ ),  $T_{\text{OP}}$  is an over-polymerization threshold used to discourage excessive curing in object regions (we use  $T_{\text{OP}} = 0.3$ ), and  $T_I$  is a minimum inhibitor level desired in void regions (we use  $T_I = 0.2$ ). Relative weights of the terms can be introduced but were not necessary for our experiments.

In all subsequent experiments, we minimize Eq. 9 with L-BFGS over the phase patterns  $\{\varphi_j\}$ , using the coupled optical and chemical forward model. Note that in our simulations we operate with normalized (dimensionless) inhibitor concentrations; consequently, the thresholds (e.g.,  $T_P, T_{\text{OP}}, T_I$ ) are selected empirically to yield stable printing outcomes. This is common practice in VAM/TVAM-style inverse design and avoids requiring absolute calibration of absorbed energy (laser power) and all reaction-rate constants.

## 4 RESULTS AND DISCUSSION

In this section, we show that inhibitor diffusion degrades print fidelity for small features, and that this degradation can be partially mitigated by chemistry-aware hologram optimization. We further demonstrate that adding TEMPO, a less diffusive inhibitor, improves print quality (at the cost of increased required dose), and we validate these effects experimentally in 2D and 3D.

To facilitate direct comparison across all experiments and simulations, we use a fixed optical configuration and a consistent set of reconstruction and optimization parameters summarized in Table 1. Unless otherwise stated, all results in this section use these settings.

Based on the above configuration, the diffraction-limited lateral resolution (Abbe limit) is approximately  $1.7 \mu\text{m}$ . The corresponding axial extent of a diffraction-limited focus is on the order of  $50 \mu\text{m}$  under our effective NA; for extended objects, axial resolution is further degraded by the missing-cone limitation inherent to single-axis projection (Appendix G).

For each set of prints, laser power is empirically tuned within  $80 \mu\text{W}$  to  $400 \mu\text{W}$  to maximize print fidelity. Such calibration is standard in VAM, since the effective polymerization threshold depends on a nonlinear interplay between optical dose and the initial chemical state of the resin. Unless otherwise stated, 2D images are acquired through the same objective used for printing, using oblique illumination from below to enhance contrast.

Table 1. Simulation and experimental parameters used throughout Sec. 4.

Fourier lens focal length $f_{\text{FL}}$	200 mm
Tube lens focal length $f_{\text{TL}}$	100 mm
Objective lens focal length $f_{\text{OL}}$	20 mm
Wavelength $\lambda$	405 nm
SLM pixel pitch $\Delta x$	$8 \mu\text{m}$
SLM resolution (used) $N \times N$	$1200 \times 1200$
Effective numerical aperture NA = $\frac{N \Delta x f_{\text{TL}}}{2 f_{\text{FL}} f_{\text{OL}}}$	0.12
Printing-plane pixel size $\Delta x_P$	$1.6875 \mu\text{m}$
Printing-plane crop (off-axis)	$500 \text{ px} \times 500 \text{ px}$ ( $844 \mu\text{m} \times 844 \mu\text{m}$ )
Optimization method / iterations	L-BFGS / 100–400
Resin refractive index $n$	1.4803
Absorption coefficient $\mu$	$0.062 \frac{1}{\text{mm}}$
Total exposure time $T_{\text{exp}}$	8 s
Number of time-multiplexed holograms $K$	20
Number of axial planes (simulation)	10–30
Axial extent (simulation/print)	2 mm to 3 mm
Laser power (experiment)	$80 \mu\text{W}$ to $400 \mu\text{W}$

### 4.1 Oxygen diffusion correction

We evaluate how oxygen transport affects print fidelity by comparing two optimization settings: (i) an optical-only model that neglects oxygen diffusion and (ii) a diffusion-aware model that explicitly accounts for oxygen depletion and diffusion during exposure. Because radicals are generated with a spatially varying 3D distribution, oxygen is depleted non-uniformly, creating concentration gradients that drive diffusive replenishment and can blur fine features.

Figure 4 summarizes the resulting forward-model predictions. When diffusion is ignored (top row), the optimization produces illumination patterns that deplete oxygen almost everywhere, including in intended void regions, which reduces inhibition and causes unintended polymerization. In contrast, diffusion-aware optimization (bottom row) reshapes the projected intensity to maintain higher inhibitor levels in void regions while still depleting oxygen within the target geometry, improving the separation between object and void distributions and yielding a more faithful thresholded reconstruction.

Overall, incorporating oxygen diffusion into the inverse design mitigates diffusion-induced artifacts which is consistent with prior observations in TVAM [Orth et al. 2023], although very fine features remain sensitive to inhibitor transport. This motivates using less diffusive inhibitors (e.g., TEMPO) and/or shorter exposure times to reduce the effective diffusion length  $\ell \propto \sqrt{D T}$ .

### 4.2 Experimental diffusion coefficient measurement

The diffusion kernel in the forward model depends on material and environmental parameters (e.g., resin viscosity, temperature, and composition). We therefore require an experimental calibration of the oxygen diffusion coefficient for the specific resin used in this work.

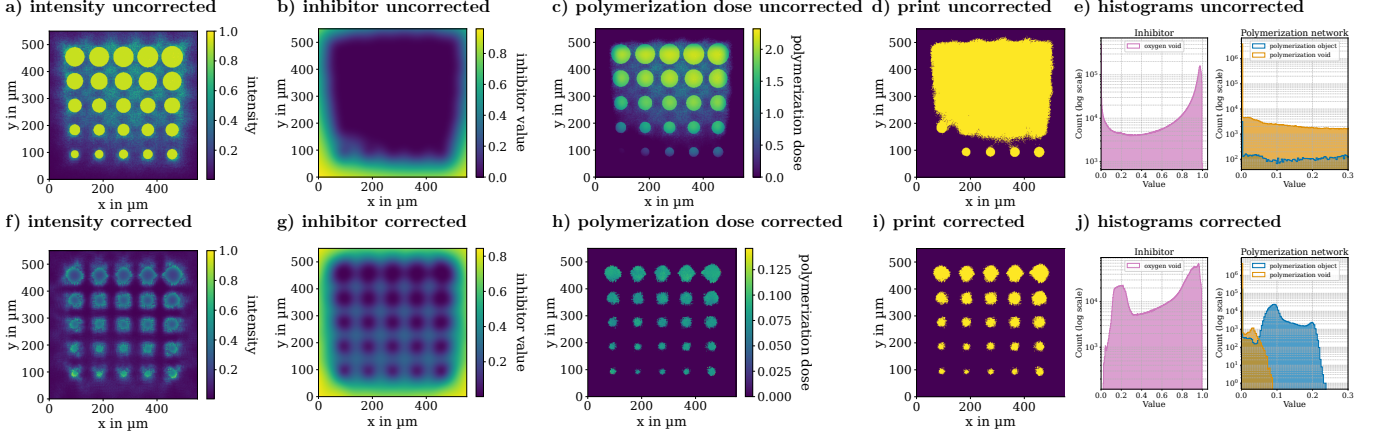


Fig. 4. Impact of oxygen diffusion on inverse-designed dose patterns. We compare holograms optimized *without* diffusion (top row) and *with* diffusion-aware optimization (bottom row), using  $D_{O_2} = 200 \frac{\mu\text{m}^2}{\text{s}}$ . **a,f**) projected intensity (slice), **b,g**) oxygen concentration after exposure, **c,h**) accumulated polymerization dose, **d,i**) thresholded print prediction, and **e,j**) histograms of oxygen (pink) and polymerization values for object (blue) and void (orange) voxels. Neglecting diffusion depletes oxygen throughout the volume and reduces class separation, leading to unintended curing in void regions; diffusion-aware optimization preserves inhibitor in voids and yields a cleaner thresholded reconstruction.

To estimate  $D_{O_2}$ , we fabricate a set of 2D test structure consisting of 25 cylindrical pillars with varying diameters (Figure 5). The diameters are ranging from  $30 \mu\text{m}$  to  $80 \mu\text{m}$  in steps of  $2 \mu\text{m}$ . For a range of candidate diffusion coefficients, we (i) optimize the projected illumination patterns using the diffusion-aware simulation model and (ii) project the resulting patterns into the prepared resin under identical experimental conditions. Figure 5a) shows an example of an optimized intensity distribution for an assumed diffusion coefficient of  $D = 10 \frac{\mu\text{m}^2}{\text{s}}$ , which is predicted in simulation to yield the printed structure shown in Figure 5b).

Experimentally, however, the corresponding projection produces the print shown in Figure 5c), acquired with a widefield camera imaging the resin container from above. The observed mismatch between simulation and experiment indicates that  $D = 10 \frac{\mu\text{m}^2}{\text{s}}$  underestimates oxygen transport in our resin. Notably, the smallest pillar is entirely missing. For  $D_{O_2} = 90 \frac{\mu\text{m}^2}{\text{s}}$  we can see, that the smallest pillars are still underpolymerized. Small features are especially affected by diffusion and hence are better suited to estimate a rough value of the diffusion coefficient.

We repeat this procedure for diffusion coefficients in the range  $D_{O_2} = 90 \frac{\mu\text{m}^2}{\text{s}}$  to  $D_{O_2} = 280 \frac{\mu\text{m}^2}{\text{s}}$ . A best-match estimate is obtained by visually comparing experimental prints to their simulated counterparts across the full pillar set. Using this comparison, we find that  $D_{O_2} = (230 \pm 50) \frac{\mu\text{m}^2}{\text{s}}$  provides the most consistent agreement. Smaller diffusion coefficients (e.g.,  $D_{O_2} = 90 \frac{\mu\text{m}^2}{\text{s}}$ ) tend to underpolymerize the smallest pillars, whereas larger values overcompensate diffusion and degrade feature fidelity. Because the present matching criterion is based on visual assessment rather than an automated metric, we report a conservative uncertainty of  $\pm 50 \frac{\mu\text{m}^2}{\text{s}}$ . This value is also in agreement with a quantitative experimental measurement in Appendix C of different pillar diameters. More acc-

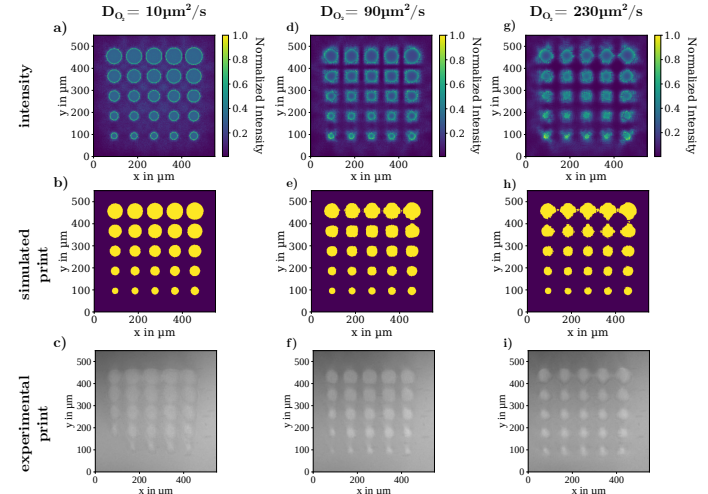


Fig. 5. Experimental calibration of the oxygen diffusion coefficient. **First row**) Example optimized projected intensity for a candidate diffusion coefficient. **Second row**) Corresponding simulated print outcome. **Third row**) Experimental print imaged from above in a widefield configuration.

urate chemical diffusion measurements also require precise optical aberration correction as otherwise it is unclear whether the dominating error comes from a mismatch in the diffusion coefficient or whether it is aberration induced.

#### 4.3 TEMPO as additional inhibitor

Previous results in TVAM have demonstrated that adding TEMPO as a secondary inhibitor significantly improves printability [Toombs et al. 2022; Thijssen et al. 2024]. Qualitatively, this benefit is attributed to the larger molecular size of TEMPO compared to oxygen,

which results in lower diffusivity and helps preserve sharp polymerization boundaries.

In this section, we incorporate quantitative modeling of TEMPO into the SHVAM inverse design framework and validate its impact through simulation and experiment. We utilize the resin formulation described in Appendix B, with relative concentrations of oxygen and TEMPO determined experimentally as detailed in Appendix D.

To assess the impact of inhibitor diffusion on lateral resolution, we designed a stress test consisting of a dense array of closely spaced pillars (85  $\mu\text{m}$  spacing, 80  $\mu\text{m}$  diameter). The results are summarized in Figure 6.

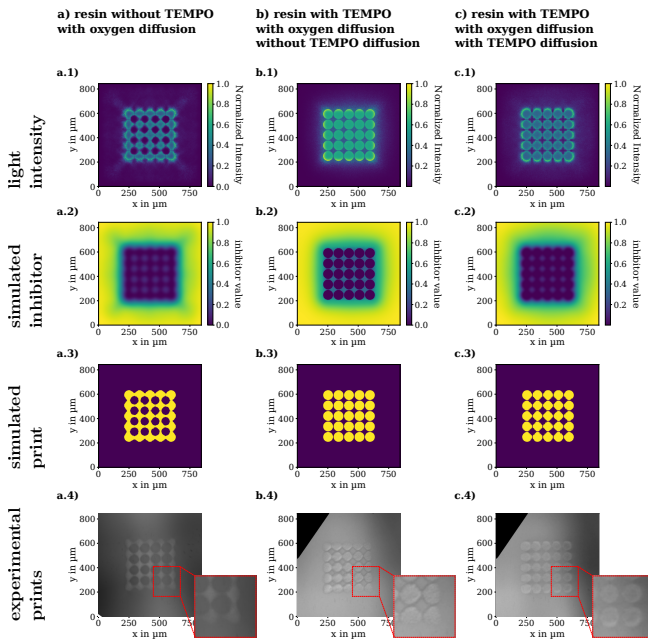


Fig. 6. Lateral resolution test comparing different inhibitor configurations: **a)** oxygen only (with diffusion correction), **b)** oxygen and TEMPO (without TEMPO diffusion modeling), and **c)** oxygen and TEMPO (with optimized diffusion coefficients). Each row displays: **1)** projected light intensity, **2)** final inhibitor concentration, **3)** simulated print outcome, and **4)** experimental result.

First, we examine a resin containing only oxygen, optimized with oxygen diffusion correction (Figure 6a). Although the projected intensity (Figure 6a.1) attempts to compensate for blur, the high diffusivity of oxygen results in a final inhibitor concentration field with poor contrast (Figure 6a.2). Consequently, the inhibitor is depleted across the inter-pillar gaps, leading to merged features in both the simulation (Figure 6a.3) and the experiment (Figure 6a.4). This confirms that even with algorithmic correction, oxygen diffusion limits the achievable pitch of dense structures.

Next, we introduce TEMPO into the resin but neglect its diffusion in the optimization model (Figure 6b). The experimental print (Figure 6b.4) shows a marked improvement in structure definition compared to the oxygen-only case, confirming the chemical benefit of TEMPO. However, because the optimization assumes TEMPO is

stationary, it fails to account for the slight diffusion that does occur. As a result, the outer pillars are under-polymerized and appear incomplete or missing in the experimental result.

Finally, we optimize the patterns using the full coupled model with experimentally tuned diffusion coefficients of  $D_{\text{O}_2} = 230 \frac{\mu\text{m}^2}{\text{s}}$  and  $D_{\text{TEMPO}} = 110 \frac{\mu\text{m}^2}{\text{s}}$  (Figure 6c). By explicitly accounting for the transport of both inhibitors, the optimizer boosts the dose at the boundaries to counteract dilution. The resulting experimental print (Figure 6c.4) shows the best agreement with the target design, with the boundary pillars fully preserved.

While eliminating oxygen entirely to rely solely on TEMPO would theoretically yield superior results, preparing oxygen-free resins requires inert gas environments or vacuum processing, which significantly increases experimental complexity. Also, in cell-laden bioresins, adequate oxygen availability is required to prevent hypoxia.

These results highlight that while diffusion-aware optimization can extend the resolution limits of VAM, fundamental physical constraints remain. Reducing the effective diffusion length would require, for example, resins with significantly higher viscosity (lowering  $D$ ) or faster printing systems (lowering  $T_{\text{print}}$ ). However, high viscosity complicates handling, and since the diffusion length scales as  $\ell \propto \sqrt{D \cdot T_{\text{print}}}$ , order-of-magnitude improvements in resolution will likely require substantial reductions in either the diffusion coefficient or the exposure time. Alternatively, more complex photochemical reaction mechanisms could be designed to mitigate these limitations.

#### 4.4 3D prints

As final experiments, we demonstrate simple 3D prints.

Due to the comparatively low numerical aperture of our projection optics ( $\text{NA} = 0.12$ ), the axial confinement of the optical field is limited, resulting in poor axial resolution (i.e., a large depth-of-focus). Consequently, we restrict ourselves to objects without strong fine-scale variations along the optical axis. For a theoretical discussion on printing with high NA systems, see Appendix H.

*Hollow, conical shaped structures.* As a first validation, we fabricated a set of hollow and solid conical structures aligned along the optical axis. The results are presented in Figure 7. We compare two optimization strategies: one based on a purely wave-optical model (neglecting chemistry, left column) and one incorporating our coupled diffusion model (right column). To provide a fair comparison, the predicted outcomes for both strategies shown in Figure 7a and Figure 7b are simulated using the full optical-chemical forward model.

While patterns optimized solely with the wave-optical model reproduce the gross geometry, they suffer from reduced fidelity; specifically, internal hollow channels are partially occluded and sharp corners appear rounded (see Figure 7c,d). Quantitative measurements in Figure 7e,f confirm this loss of resolution: the experimental side length of the triangle was  $(160 \pm 10) \mu\text{m}$  against a target of 245  $\mu\text{m}$ , while the cone diameter was  $(250 \pm 10) \mu\text{m}$  against a target of 280  $\mu\text{m}$ . These experimental deviations are consistent with the outcome predicted by the chemical simulation in Figure 7a.

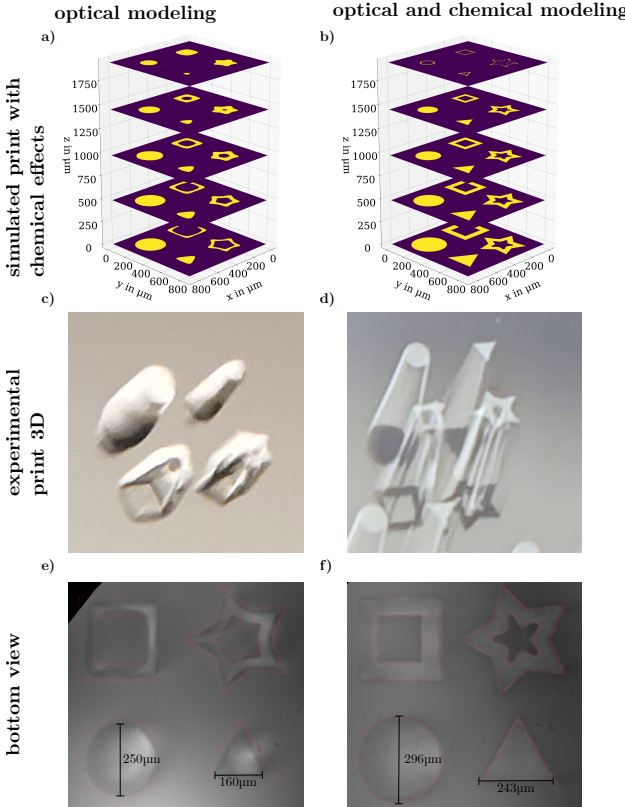


Fig. 7. Comparison of 3D conical structures fabricated using optical-only optimization (left column) versus our diffusion-aware approach (right column). **a, b)** Simulated print predictions evaluated using the full chemical forward model for **a)** optical-only patterns and **b)** chemically-optimized patterns. **c, d)** Experimental 3D views of the printed structures. **e, f)** Experimental 2D cross-sectional microscopy images (bottom view). Red dashed lines indicate the target design. The optical-only optimization **c, e)** results in feature shrinkage and occlusion of the central hollow channels (triangle side length: 160  $\mu\text{m}$ ). In contrast, the chemically coupled optimization **d, f)** successfully compensates for diffusion, achieving better dimensions (triangle side length: 243  $\mu\text{m}$ ) and preserving the hollow core structure.

In contrast, when diffusion effects are explicitly included in the inverse design, the hollow cores within the square- and star-shaped cones are preserved (see Figure 7d,f), yielding prints that closely match the intended topology. This improvement is confirmed quantitatively, with the triangle side length and cone diameter measured at  $(243 \pm 10) \mu\text{m}$  and  $(296 \pm 10) \mu\text{m}$ , respectively.

Note that for all experimental prints, the global laser power was finely tuned to achieve the optimal trade-off between solidification and feature resolution.

**High-resolution print.** To probe the resolution limits of our system, we fabricated a hollow, conical star structure, shown in Figure 8. The target geometry (Figure 8a) contains fine features designed to test lateral confinement. The corresponding experimental result (Figure 8b) demonstrates that SHVAM can resolve features on the order of 10  $\mu\text{m}$  with a total print time of just 1.5 s.

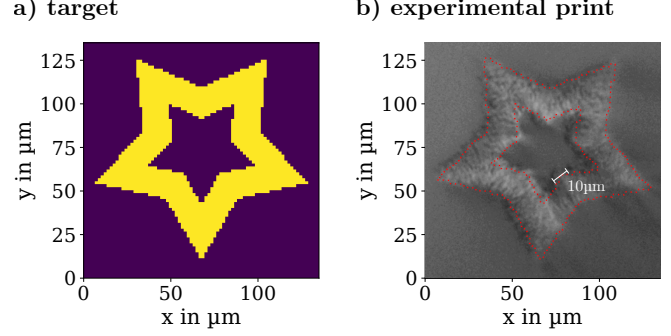


Fig. 8. High-resolution printing demonstration. **a)** 2D cross section of the target hollow star geometry. **b)** Optical microscopy image of the printed structure, fabricated in 1.5 s. The system resolves lateral features of approximately 10  $\mu\text{m}$ , though some surface granularity remains due to optical speckle.

The printed structure exhibits a granular texture, which we attribute to speckle noise in the time-integrated dose distribution. Notably, our simulations based on the same optical model predict that even finer features are attainable (see Appendix F). This suggests that the current experimental resolution is limited primarily by projection quality (specifically speckle contrast and system aberrations) rather than by the inverse design formulation itself. Future improvements in holographic calibration (e.g., [Peng et al. 2020]) could reduce these artifacts and allow the system to approach the theoretical resolution limits predicted by simulation.

**High-throughput printing.** Finally, we demonstrate the high-throughput capabilities of SHVAM. Figure 9 displays a  $3 \times 3$  grid of three-legged structures fabricated simultaneously in a single exposure sequence. While the low numerical aperture of our current objective limits the axial sharpness at the tips, the system successfully produces the entire array with consistent geometry. The total print time for this array was 8 s.

**Printing speed.** Based on our experimentally demonstrated field of view of 800  $\mu\text{m}$  (with  $\sim 10 \mu\text{m}$  lateral resolution) and a printable depth of 3 mm (with  $\sim 150 \mu\text{m}$  axial resolution), we estimate a total addressable volume of approximately 128 000 effective voxels. Given the print duration, this corresponds to a continuous production rate of approximately 16 000 voxels/s. However, by using piston based phase light modulators (PLMs) or digital micromirror devices (DMDs) with Lee hologram projections [Álvarez Castaño et al. 2025], pattern display rates can be increased from the current 40 Hz to  $\gg 1000$  Hz. Additionally, by also increasing the laser power from around 400  $\mu\text{W}$  (this work) to mW regimes, printing rates of  $> 1\,000\,000$  voxels/s could be achieved.

## 5 CONCLUSION

In this work, we introduced *Single-View Holographic Volumetric Additive Manufacturing* (SHVAM), a computational fabrication framework that synthesizes 3D micro-structures from a single optical axis

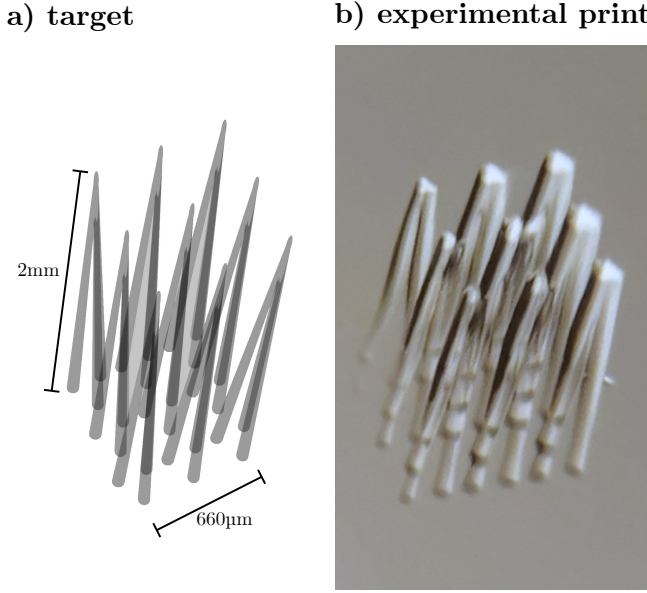


Fig. 9. High-throughput fabrication demonstration. A  $3 \times 3$  array of hollow pyramids printed simultaneously in 8 s. Despite the axial resolution limits imposed by the low-NA optics (visible as blunted tips), the system achieves parallel fabrication of multiple complex micro-structures across the full 800  $\mu\text{m}$  field of view. **a)** shows the target geometry. **b)** displays the final print.

without moving parts. By shifting the complexity of volumetric shaping from mechanical hardware to algorithmic design, SHVAM utilizes time-multiplexed phase holography to sculpt time-integrated (effectively incoherent) dose distributions within a photosensitive resin. Central to our approach is a coupled differentiable forward model that integrates wave optics with a simplified inhibition-diffusion photochemistry surrogate.

Our experiments demonstrate that at the micro-scale, optical optimization alone is insufficient: transport of inhibitors (oxygen and TEMPO) significantly alters the effective printed geometry. By explicitly modeling these chemical dynamics within the inverse design loop, we can pre-compensate diffusion-driven blur and improve print fidelity. We validate this approach by fabricating 3D geometries with lateral features down to 10  $\mu\text{m}$  in exposure times as short as 1.5 s. Moreover, higher-refresh-rate modulators (e.g., piston-based phase light modulators) could enable sub-second exposures, increasing throughput while reducing diffusion-induced degradation by shortening the relevant transport time.

Our current prototype highlights key trade-offs inherent to single-view projection, including limited axial resolutions due to the low effective NA as well as artifacts from coherent projection (speckle and aberrations). While speckle and aberrations can be mitigated through improved holographic calibration and system characterization, improving axial resolution in a single-view architecture will require higher-NA optics (with the corresponding reduction in field of view, see Appendix H) and/or additional degrees of freedom.

More broadly, our results suggest that coupling wave-optical inverse design with inhibition and diffusion modeling provides a practical path toward higher-fidelity volumetric microfabrication. Crucially, the photochemical formulation presented here is agnostic to the optical delivery method and can be readily integrated into other volumetric printing approaches – such as TVAM – to push resolution beyond current optical-only optimization limits.

## ACKNOWLEDGMENTS

During the preparation of this work, the authors used generative AI models to enhance the quality of the work. In particular, AI models were used to write source code and to improve the grammar, spelling, and clarity of the manuscript’s text (including this sentence). This project has received funding from the Swiss National Science Foundation 2000-1-240074 under grant number 10007068 - *Neural precision holographic volumetric additive manufacturing* and from the Swiss National Science Foundation Return CH Post-doc.Mobility P5R5-3\_235066 (R.R.). We appreciate discussions with Jonathan Dong on the optical theory.

## REFERENCES

Paulina Nuñez Bernal, Paul Delrot, Damien Loterie, Yang Li, Jos Malda, Christophe Moser, and Riccardo Levato. 2019. Volumetric bioprinting of complex living-tissue constructs within seconds. *Advanced materials* 31, 42 (2019), 1904209. <https://doi.org/10.1002/adma.201904209>

Indrasen Bhattacharya, Joseph Toombs, and Hayden Taylor. 2021. High fidelity volumetric additive manufacturing. *Additive Manufacturing* 47 (2021), 102299. <https://doi.org/10.1016/j.addma.2021.102299>

M. Campbell, D. N. Sharp, M. T. Harrison, R. G. Denning, and A. J. Turberfield. 2000. Fabrication of photonic crystals for the visible spectrum by holographic lithography. *Nature* 404, 6773 (March 2000), 53–56. <https://doi.org/10.1038/35003523>

Suyeon Choi, Manu Gopakumar, Yifan Peng, Jonghyun Kim, and Gordon Wetzstein. 2021. Neural 3D holography: learning accurate wave propagation models for 3D holographic virtual and augmented reality displays. *ACM Trans. Graph.* 40, 6, Article 240 (Dec. 2021), 12 pages. <https://doi.org/10.1145/3478513.3480542>

S. Scott Crump. 1992. Apparatus and method for creating three-dimensional objects. Uzi Efron. 1994. *Spatial Light Modulator Technology: Materials, Devices and Applications*. Marcel Dekker, Inc., USA.

Joseph W Goodman. 2017. *Introduction to Fourier Optics* (4th ed.). W. H. Freeman.

Larry J Hornbeck. 1997. Digital light processing for high-brightness high-resolution applications. In *Projection Displays III*, Vol. 3013. SPIE, 27–40.

Charles W. Hull. 1986. Apparatus for production of three-dimensional objects by stereolithography.

K. Ikuta and K. Hirowatari. 1993. Real three dimensional micro fabrication using stereo lithography and metal molding. In [1993] *Proceedings IEEE Micro Electro Mechanical Systems*. 42–47. <https://doi.org/10.1109/MEMSYS.1993.296949>

Brett E Kelly, Indrasen Bhattacharya, Hossein Heidari, Maxim Shusteff, Christopher M Spadaccini, and Hayden K Taylor. 2019. Volumetric additive manufacturing via tomographic reconstruction. *Science* 363, 6431 (2019), 1075–1079. <https://doi.org/10.1126/science.aau7114>

Hideo Kodama. 1981. Automatic method for fabricating a three-dimensional plastic model with photo-hardening polymer. *Review of Scientific Instruments* 52, 11 (Nov. 1981), 1770–1773. <https://doi.org/10.1063/1.1136492>

C. Li. 2024. *Developments of Multi-beam 3D Holographic Lithography for Volumetric Additive Manufacturing*. Ph.D. Dissertation. UC Berkeley. <https://escholarship.org/uc/item/3sb4f4qg>

Chi Chung Li, Joseph Toombs, Vivek Subramanian, and Hayden K. Taylor. 2024. Intensity-coupled multi-beam phase retrieval for holographic volumetric additive manufacturing. *Opt. Express* 32, 26 (Dec 2024), 47620–47637. <https://doi.org/10.1364/OE.544010>

Dajun Lin, Xiaofeng Chen, Connor O. Dea, Ji-Won Kim, Keldy S. Mason, Kwong Sang Lee, Apratim Majumder, Chih-Hao Chang, Michael Cullinan, Zachariah A. Page, and Rajesh Menon. 2026. Single-exposure holographic 3D printing via inverse-designed phase masks. *arXiv:2601.06614 [physics.optics]* <https://arxiv.org/abs/2601.06614>

Dong C. Liu and Jorge Nocedal. 1989. On the limited memory BFGS method for large scale optimization. *Mathematical Programming* 45, 1 (Aug. 1989), 503–528. <https://doi.org/10.1007/BF01589116>

Damien Loterie, Paul Delrot, and Christophe Moser. 2020. High-resolution tomographic volumetric additive manufacturing. *Nature Communications* 11, 11 (Feb. 2020), 852. <https://doi.org/10.1038/s41467-020-14630-4>

Shoji Maruo, Osamu Nakamura, and Satoshi Kawata. 1997. Three-dimensional micro-fabrication with two-photon-absorbed photopolymerization. *Opt. Lett.* 22, 2 (Jan 1997), 132–134. <https://doi.org/10.1364/OL.22.000132>

Kyoji Matsushima and Tomoyoshi Shimobaba. 2009. Band-Limited Angular Spectrum Method for Numerical Simulation of Free-Space Propagation in Far and Near Fields. *Optics Express* 17, 22 (Oct. 2009), 19662–19673. <https://doi.org/10.1364/OE.17.019662>

Jerome Mertz. 2019. *Introduction to Optical Microscopy* (2 ed.). Cambridge University Press.

Christophe Moser, Felix Wechsler, and Maria Isabel Alvarez Castaño. [n. d.]. System and method for high throughput and high-resolution volumetric additive manufacturing using time multiplexed computer-generated holograms. <https://patents.google.com/patent/WO2025223658A1/en> Status: Pending.

Baptiste Nicolet, Felix Wechsler, Jorge Madrid-Wolff, Christophe Moser, and Wenzel Jakob. 2024. Inverse Rendering for Tomographic Volumetric Additive Manufacturing. *ACM Trans. Graph.* 43, 6 (Nov. 2024), 228:1–228:17. <https://doi.org/10.1145/3687924>

Antony Orth, Daniel Webber, Yujie Zhang, Kathleen L. Sampson, Hendrick W. de Haan, Thomas Lacelle, Rene Lam, Daphne Solis, Shyamaleeswari Dayanandan, Taylor Waddell, Tasha Lewis, Hayden K. Taylor, Jonathan Boisvert, and Chantal Paquet. 2023. Deconvolution volumetric additive manufacturing. *Nature Communications* 14, 11 (July 2023), 4412. <https://doi.org/10.1038/s41467-023-39886-4> 0 citations (Crossref) [2023-08-15].

Yifan Peng, Suyeon Choi, Nitish Padmanabhan, and Gordon Wetzstein. 2020. Neural holography with camera-in-the-loop training. *ACM Trans. Graph.* 39, 6, Article 185 (Nov. 2020), 14 pages. <https://doi.org/10.1145/3414685.3417802>

Charles M. Rackson, Kyle M. Champlie, Joseph T. Toombs, Erika J. Fong, Vishal Bansal, Hayden K. Taylor, Maxim Shusteff, and Robert R. McLeod. 2021. Object-space optimization of tomographic reconstructions for additive manufacturing. *Additive Manufacturing* 48 (Dec. 2021), 102367. <https://doi.org/10.1016/j.addma.2021.102367>

Maxim Shusteff, Allison E. M. Browar, Brett E. Kelly, Johannes Henriksson, Todd H. Weisgraber, Robert M. Panas, Nicholas X. Fang, and Christopher M. Spadaccini. 2017. One-step volumetric additive manufacturing of complex polymer structures. *Science Advances* 3, 12 (Dec. 2017), eaao5496. <https://doi.org/10.1126/sciadv.aao5496>

Paul Somers, Sebastian Koch, Pascal Kiefer, Maryna L. Meretska, and Martin Wegener. 2024. Holographic multi-photon 3D laser nanoprinting &#x2013; at the speed of light: opinion. *Opt. Mater. Express* 14, 10 (Oct 2024), 2370–2376. <https://doi.org/10.1364/OME.538751>

Quinten Thijssen, Antonio Jaén Ortega, Roniérík Pioli Vieira, and Sandra Van Vlierberghe. 2024. Radical inhibition in tomographic volumetric 3D printing for thiol-ene photoresists: From photoredox to printability. *Reactive and Functional Polymers* 205 (2024), 106096. <https://doi.org/10.1016/j.reactfunctpolym.2024.106096>

Joseph T. Toombs, Manuel Luitz, Caitlyn C. Cook, Sophie Jenne, Chi Chung Li, Bastian E. Rapp, Frederik Kotz-Helmer, and Hayden K. Taylor. 2022. Volumetric additive manufacturing of silica glass with microscale computed axial lithography. *Science* 376, 6590 (April 2022), 308–312. <https://doi.org/10.1126/science.abm6459>

John R. Tumbleston, David Shirvanyants, Nikita Ermoshkin, Rima Januszewicz, Ashley R. Johnson, David Kelly, Kai Chen, Robert Pischmidt, Jason P. Rolland, Alexander Ermoshkin, Edward T. Samulski, and Joseph M. DeSimone. 2015. Continuous liquid interface production of 3D objects. *Science* 347, 6228 (2015), 1349–1352. <https://doi.org/10.1126/science.aaa2397>

Felix Wechsler, Carlo Gigli, Jorge Madrid-Wolff, and Christophe Moser. 2024. Wave optical model for tomographic volumetric additive manufacturing. *Optics Express* 32, 8 (April 2024), 14705–14712. <https://doi.org/10.1364/OE.521322>

Felix Wechsler, Viola Sgarminato, Riccardo Rizzo, Baptiste Nicolet, Wenzel Jakob, and Christophe Moser. 2025. Overprinting with Tomographic Volumetric Additive Manufacturing. [arXiv:2507.13842 \[physics.optics\]](https://arxiv.org/abs/2507.13842) <https://arxiv.org/abs/2507.13842>

Todd H Weisgraber, Martin P de Beer, Sijia Huang, John J Karnes, Caitlyn C Cook, and Maxim Shusteff. 2023. Virtual Volumetric Additive Manufacturing (VirtualVAM). *Advanced Materials Technologies* 8, 23 (2023), 2301054. <https://doi.org/10.1002/admt.202301054>

Leran Zhang, Chaowei Wang, Chenchu Zhang, Yuhang Xue, Zhaohui Ye, Liqun Xu, Yanlei Hu, Jiawen Li, Jiaru Chu, and Dong Wu. 2024. High-Throughput Two-Photon 3D Printing Enabled by Holographic Multi-Foci High-Speed Scanning. *Nano Letters* 24, 8 (2024), 2671–2679. <https://doi.org/10.1021/acs.nanolett.4c00505> PMID: 38375804 arXiv:<https://doi.org/10.1021/acs.nanolett.4c00505> PMID: 38375804

Yujie Zhang, Hendrick De Haan, Katherine Houlahan, Kathleen L. Sampson, Daniel Webber, Antony Orth, Thomas Lacelle, Liliana Gaburici, Rene Lam, Bhavana Deore, and Chantal Paquet. 2025. Impact of oxygen inhibition on (meth)acrylate photopolymerization in tomographic volumetric printing. *Additive Manufacturing* 109 (July 2025), 104844. <https://doi.org/10.1016/j.addma.2025.104844>

Cheng Zheng, Guangyuan Zhao, and Peter So. 2023. Close the Design-to-Manufacturing Gap in Computational Optics with a ‘Real2Sim’ Learned Two-Photon Neural Lithography Simulator. In *SIGGRAPH Asia 2023 Conference Papers* (Sydney, NSW, Australia) (SA ’23). Association for Computing Machinery, New York, NY, USA, Article 56, 9 pages. <https://doi.org/10.1145/3610548.3618251>

Maria Isabel Álvarez Castaño, Andreas Gejl Madsen, Jorge Madrid-Wolff, Viola Sgarminato, Antoine Boniface, Jesper Glückstad, and Christophe Moser. 2025. Holographic tomographic volumetric additive manufacturing. *Nature Communications* 16, 1 (Feb. 2025), 1551. <https://doi.org/10.1038/s41467-025-56852-4>

## A OPTICAL SETUP

A 405 nm laser (Coherent OBIS LX SF 405-40, narrow-linewidth, single-longitudinal-mode) was used as the light source. The beam was collimated onto the spatial light modulator (SLM). A half-wave plate was used to align the beam polarization with the SLM.

The SLM was a Meadowlark E-19x12-400-800-HDM8 with a resolution of 1920 × 1200 pixels and a pixel pitch of 8 μm. A Fourier lens with focal length  $f_{FL} = 200$  mm (ACT508-200-A-ML, Thorlabs) was used, and an off-axis diffraction order was selected using a circular aperture. A tube lens with focal length  $f_{TL} = 100$  mm (AC508-100-A-ML, Thorlabs) relayed the beam to the objective.

For focusing into the resin, we used an objective lens with focal length  $f_{OL} = 20$  mm (M Plan APO 10x, Mitutoyo), with a theoretical numerical aperture of  $NA = 0.28$ . In our setup, the back aperture of the objective was intentionally underfilled, resulting in a lower effective NA to increase the field of view.

For imaging, the same microscope objective was used in combination with a dichroic mirror to block the blue illumination light partially. The imaging arm employed a 120 mm tube lens and a CMOS camera (Basler ace 2 a2A4504-18umPRO).

## B RESIN PREPARATION

We prepared the resin by mixing DUDMA (Sigma-Aldrich, USA) and PEGDA 700 (Sigma-Aldrich, USA) at a 4:1 weight ratio. As the photoinitiator, we used diphenyl(2,4,6-trimethylbenzoyl)phosphine oxide (TPO, 97 %; Sigma-Aldrich), which was first dissolved in 99 % Isopropyl alcohol (IPA) and then incorporated using a planetary mixer (KK-250SE, Kurabo). As an additional inhibitor, we used 2,2,6,6-tetramethylpiperidine 1-oxyl (TEMPO, 98 %; Sigma-Aldrich); TEMPO was likewise dissolved in 99 % IPA before being mixed into the resin.

The resin had a measured refractive index of  $n = 1.4803 \pm 0.003$  and an absorption coefficient of  $\mu = 0.062 \frac{1}{\text{mm}}$ . For sample preparation, small droplets of resin were dispensed onto a microscope slide and confined with a rubber spacer ring of thickness 1.5 mm to 3 mm. A cover slip was placed on top of the ring to seal the volume. The printed volume spanned the entire gap between the glass interfaces.

## C OXYGEN DIFFUSION COEFFICIENT

In addition to the qualitative (visual) estimate reported in subsection 4.2, we perform a simple quantitative consistency check based on measured feature sizes. Specifically, we fabricate three isolated pillar targets with nominal diameters of 20 μm, 40 μm, and 60 μm. For a range of candidate oxygen diffusion coefficients  $D_{O_2}$ , we re-optimize the hologram patterns and compare the resulting simulated pillar diameters to those measured experimentally.

As shown in Figure 10, small diffusion coefficients ( $D_{O_2} \lesssim 100 \frac{\mu\text{m}^2}{\text{s}}$ ) lead to severe under-polymerization, and the smallest pillars are partially formed or missing. In contrast, diffusion coefficients in

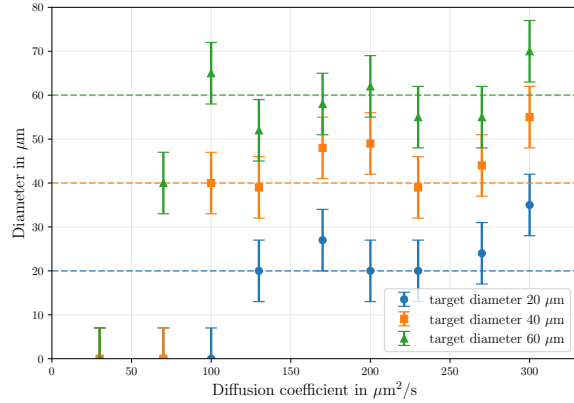


Fig. 10. Measured (experiment) pillar diameters for different assumed oxygen diffusion coefficients  $D_{O_2}$ , evaluated on pillar targets with nominal diameters of 20  $\mu\text{m}$ , 40  $\mu\text{m}$ , and 60  $\mu\text{m}$ .

the range 150  $\frac{\mu\text{m}^2}{\text{s}}$  to 270  $\frac{\mu\text{m}^2}{\text{s}}$  yield the closest agreement between simulated and experimental diameters across the three pillar sizes.

We note that diameter measurements are inherently noisy in our setup because the apparent pillar boundary depends on the chosen exposure and focus settings during imaging, introducing operator-dependent uncertainty. Given these limitations, we select  $D_{O_2} = 230 \frac{\mu\text{m}^2}{\text{s}}$  as a representative value, consistent with the estimate reported earlier.

#### D EXPERIMENTAL CHARACTERIZATION OF RELATIVE INHIBITOR CONCENTRATIONS

The base resin contained a photoinitiator (TPO) concentration of  $c_{\text{TPO}} = 1.2 \frac{\text{mmol}}{\text{dm}^3}$ . This batch was then split into two portions. To the second portion, we added 2.5 mg TEMPO to 38.46 g resin, corresponding to  $c_{\text{TEMPO}} = 0.46 \frac{\text{mmol}}{\text{dm}^3}$ .

While  $c_{\text{TEMPO}}$  is known from the preparation, the dissolved oxygen concentration in the resin is not. We therefore performed a calibration experiment to estimate  $c_{O_2}$ . Following recent work [Zhang et al. 2025], we assume that the time prior observable polymerization is dominated by inhibitor depletion and is therefore approximately proportional to the inhibitor concentration. Concretely, we varied the projected intensity and measured the exposure time until polymerization became visible. Figure 11a) illustrates the projected pattern, and Figure 11b) shows the polymerized region after several seconds of illumination. A circular disc of 600  $\mu\text{m}$  diameter was projected. The diameter was chosen to be sufficiently large to neglect inhibitor diffusion during the exposure.

Using the analytical model in [Zhang et al. 2025], we fit the oxygen concentration  $c_{O_2}$  and a correction factor  $\eta$  (absorbing error in the power measurement and quantum efficiency of TPO) to the measured exposure times. The depletion time for oxygen is

$$T_{O_2} = \frac{N_A \cdot h \cdot v \cdot c_{O_2}}{2 \cdot \eta \cdot \varepsilon \cdot I \cdot c_{\text{TPO}}}, \quad (10)$$

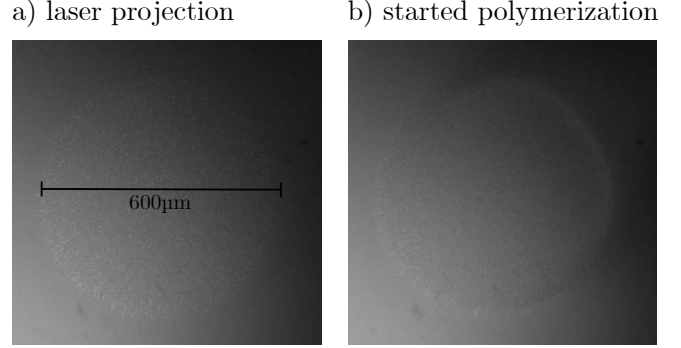


Fig. 11. Inhibitor depletion-time measurements for two resins: one containing oxygen only and one containing oxygen and TEMPO. a) Projected circular disc pattern. b) Polymerized region after several seconds of illumination. c) Measured exposure time versus projected intensity, together with the fitted model.

and for TEMPO

$$T_{\text{TEMPO}} = \frac{N_A \cdot h \cdot v \cdot c_{\text{TEMPO}}}{2 \cdot \eta \cdot \varepsilon \cdot I \cdot c_{\text{TPO}}}, \quad (11)$$

where  $N_A$  is the Avogadro constant,  $h$  is the Planck constant,  $v = 740 \text{ THz}$  is the laser frequency.  $c_{\text{TPO}} = 1.2 \frac{\text{mmol}}{\text{dm}^3}$ , and  $c_{\text{TEMPO}} = 0.46 \frac{\text{mmol}}{\text{dm}^3}$  are the concentrations of TPO, and TEMPO, respectively.  $\varepsilon = 500 \frac{\text{L}}{\text{cm} \cdot \text{mol}}$  is the molar absorption coefficient (estimated from the TPO concentration and measured absorbance), and  $I$  is the illumination intensity.

We performed two sets of time measurements for different illumination intensities:

- Resin containing oxygen only (no added TEMPO), for which we approximate the polymerization time as  $T_{O_2}$  (Eq. 10).
- Resin containing oxygen and TEMPO, for which we approximate the polymerization time as  $T_{O_2} + T_{\text{TEMPO}}$  (Eqs. 10 and 11).

Strictly, depletion time is not identical to the polymerization time; however, we use this approximation because inhibitor depletion dominates the observed delay before polymerization [Zhang et al. 2025]. The fit yields  $c_{O_2} = (0.33 \pm 0.03) \frac{\text{mmol}}{\text{dm}^3}$  and  $\eta = 0.36 \pm 0.02$ , as

shown in Figure 11c). In the simulations, we use relative (normalized) concentrations rather than absolute values. We therefore set  $c[\text{O}_2] = 1$  and  $c[\text{TEMPO}] = 1.397$ .

## E MOTIVATION TO USE SEVERAL PATTERNS

Instead of an electronically controllable SLM, one could also employ a static phase mask [Lin et al. 2026]. A key advantage of a fabricated mask is that it can be made significantly larger than the active aperture and pixel count of a single SLM, thereby relaxing constraints on the addressable spatial bandwidth.

There are, however, two fundamental disadvantages of relying on a *single* coherent phase pattern. First, a single coherent realization is more susceptible to experimentally induced coherent speckle. In contrast, displaying multiple distinct patterns and time-multiplexing them reduces speckle through temporal averaging, yielding a smoother deposited dose.

Second, and more importantly for volumetric patterning, a single 2D phase pattern cannot in general produce volumetric intensity distributions as rich as those achievable by a time-multiplexed set of patterns. The underlying reason is physical: for a monochromatic field, the complex electric field  $E(\mathbf{r})$  in the volume is constrained by the Helmholtz equation,

$$(\nabla^2 + k^2) E(\mathbf{r}) = 0, \quad (12)$$

(with  $k = 2\pi/\lambda$  in the medium). Thus, a single phase pattern defines boundary conditions at the modulator plane and generates a *single* coherent field  $E(\mathbf{r})$  in the volume, from which the intensity follows as

$$I(\mathbf{r}) = |E(\mathbf{r})|^2. \quad (13)$$

Consequently, the attainable intensity distributions are restricted to those that can arise as the squared magnitude of a Helmholtz-consistent field produced from that single boundary condition.

By contrast, time-multiplexing  $K$  phase patterns produces an *incoherent* dose accumulation (since the resin integrates intensities),

$$I(\mathbf{r}) = \sum_{k=1}^K |E_k(\mathbf{r})|^2, \quad (14)$$

where each field  $E_k(\mathbf{r})$  individually satisfies the Helmholtz equation. Importantly, the *sum of intensities* is not itself required to correspond to the intensity of any single Helmholtz solution, i.e., there does not generally exist an  $E(\mathbf{r})$  such that  $|E(\mathbf{r})|^2 = \sum_k |E_k(\mathbf{r})|^2$ . This decouples the achievable dose distribution from the constraints imposed by any single coherent field realization and constitutes a fundamental physical motivation for using multiple patterns.

To demonstrate this effect, we optimize phase patterns such that their thresholded intensity matches the target distribution shown in Figure 12a), consisting of four prisms of width 40  $\mu\text{m}$  and length 30  $\mu\text{m}$ , with a spacing of roughly 500  $\mu\text{m}$ . As loss function for the optimization, we use a threshold-inspired penalty similar to those employed throughout this work:

$$\mathcal{L} = \sum_{v \in \text{object}} 10 \cdot |\text{ReLU}(0.9 - I_v)|^2 + \sum_{v \notin \text{object}} |\text{ReLU}(I_v - 0.8)|^2, \quad (15)$$

where  $I_v$  denotes the (time-multiplexed) intensity at voxel  $v$ .

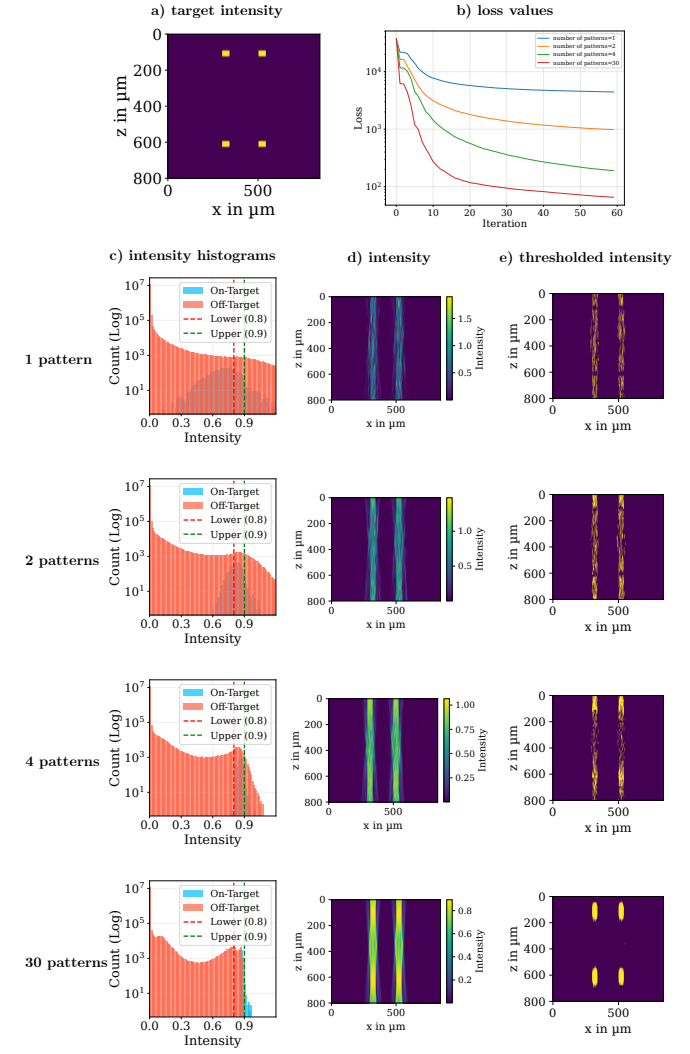


Fig. 12. Simulation results of the intensity distribution for a different amount of phase patterns. a) Target. b) Loss curves for 1, 2, 4, and 20 phase patterns. c) Intensity histograms for different pattern counts. d) Summed intensities. e) Thresholded intensities at threshold 0.843.

Performing this optimization with an L-BFGS optimizer yields the loss curves shown in Figure 12b). The resulting intensity histograms are depicted in Figure 12c), while Figure 12d) shows the summed intensities and Figure 12e) shows the corresponding thresholded intensities at threshold value 0.843.

We can clearly identify that a single phase pattern is not able to craft a 3D light intensity distribution in which laterally separated target objects remain well confined and separated in the volume. In practice, the field required to illuminate objects of this lateral extent tends to exhibit an extended axial depth-of-focus (analogous to the long Rayleigh range of a wide-waist Gaussian beam), which leads to unwanted axial spreading and overlap of the high-intensity regions.

As the number of time-multiplexed patterns increases, the projection becomes effectively more incoherent in the sense of dose

accumulation: each pattern can contribute dose to only a subset of the target voxels, while depositing less dose elsewhere. Only their sum yields a sufficiently selective 3D intensity distribution such that the thresholded result matches the desired objects. With rapidly refreshing displays such as piston based phase light modulators (PLM) (refresh rates  $\gg 1000$  Hz) the spatial bandwidth can also be much further increased beyond the one of a single phase mask.

## F CURRENT RESOLUTION LIMITS

Figure 13 shows a challenging hollow conical target that probes the practical resolution limits of our current SHVAM prototype. In simulation, the coupled forward model predicts that the structure should be printable with the desired internal hollow star.

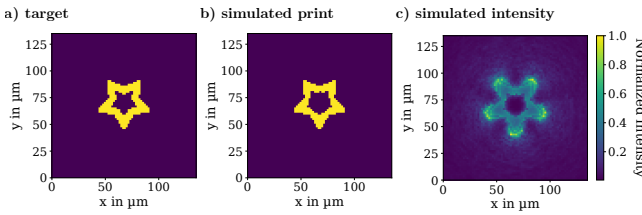


Fig. 13. Resolution limits in simulation. **a)** Target geometry. **b)** Predicted print outcome (simulation). **c)** Corresponding optimized projection intensity.

Experimentally, however, we were not able to reliably preserve the full hole diameter, and the hollow core partially closes. We attribute this discrepancy primarily to residual coherent speckle and unmodeled system imperfections in the projection path, including SLM-related artifacts (e.g., phase nonidealities) and small optical misalignments or aberrations that are not captured in our idealized wave-optical model.

## G MISSING CONE

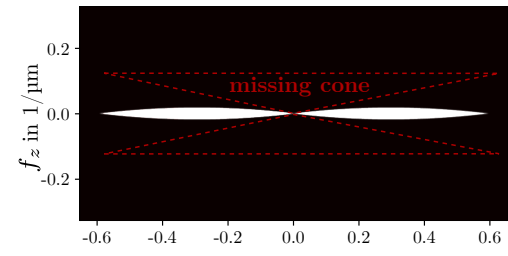
The limited axial resolution of a single-axis projection geometry can be understood from its spatial-frequency support, analogous to the optical transfer function (OTF) of incoherent widefield imaging [Mertz 2019]. In this picture, the accessible 3D frequency region is given by the autocorrelation of the Ewald-sphere cap defined by the system numerical aperture (NA). Because lateral and axial frequencies scale differently, the resulting support is highly anisotropic and exhibits a characteristic *missing cone* along the axial frequency axis.

Figure 14 visualizes this frequency support (values of the  $|\text{OTF}| > 0$ ) for three numerical apertures: **a)** NA = 0.12, **b)** NA = 0.36, and **c)** NA = 0.72.

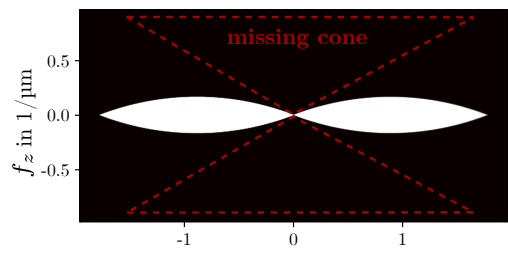
At NA = 0.12, axial frequency coverage is extremely limited, implying poor axial confinement and strong elongation of features along the optical axis. Increasing the NA to 0.36 substantially expands the accessible axial bandwidth, and NA = 0.72 provides good (though still anisotropic) coverage compared to lateral frequencies. In addition, at low lateral frequencies the axial coverage remains sparse, which particularly degrades the reproduction of objects that are thin or sharply varying along  $z$ .

This missing-cone limitation is fundamental to single-view projection and cannot be removed by optimization alone; it requires

**a) NA=0.12**



**b) NA=0.36**



**c) NA=0.72**

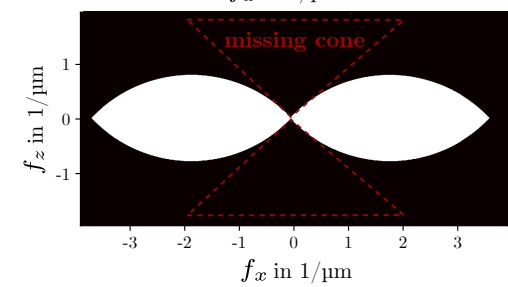


Fig. 14. Spatial-frequency support (OTF) of a single-axis projection system for **a)** NA = 0.12, **b)** NA = 0.36, and **c)** NA = 0.72. Note the different scaling of lateral and axial frequency axes. The cone-shaped gap around the axial frequency axis corresponds to missing axial information and limits axial confinement.

additional angular diversity, for example by introducing a second projection arm to fill in the missing axial frequencies.

## H HIGH-NA RESOLUTION CAPABILITIES

To assess the theoretical volumetric resolution limits of SHVAM beyond our experimental prototype, we perform simulations using higher numerical aperture (NA) configurations. For this analysis, we focus solely on the optical constraints by disabling the inhibitor diffusion model, thereby isolating the diffraction-limited performance. We select the community-standard #3DBenchy model as a challenging volumetric test target.

To ensure a fair comparison, we maintain a constant computational grid size of  $100 \times 100 \times 100$  voxels across all simulations while scaling the physical field of view inversely with the NA. This reflects the practical trade-off in microscopy where higher resolution typically necessitates a smaller field of view. We evaluate three configurations: our experimental baseline of NA = 0.12 (pixel size  $1.69 \mu\text{m}$ ), a moderate NA = 0.36 (pixel size  $0.56 \mu\text{m}$ ), and a high

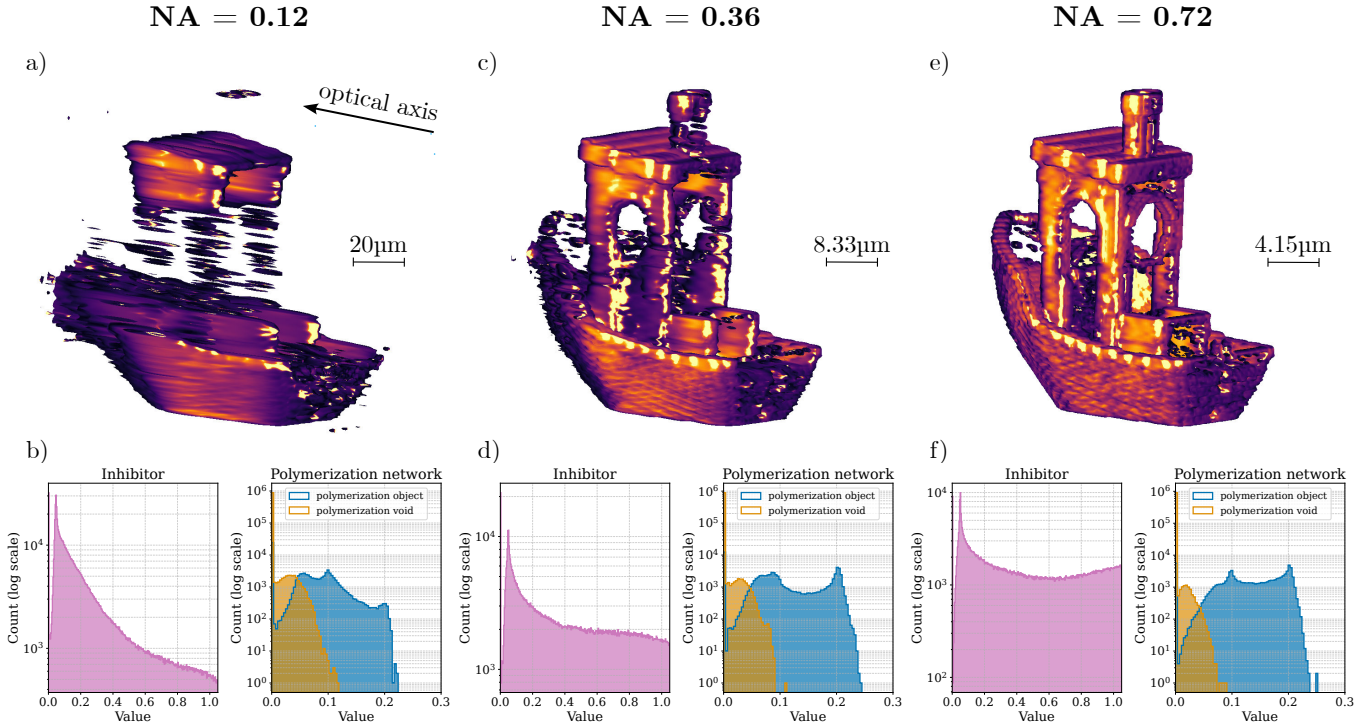


Fig. 15. Simulated print outcomes for varying Numerical Apertures (NA). **a, b**) Result and dose histogram for NA = 0.12; the object is barely recognizable due to poor axial confinement. **c, d**) Result and histogram for NA = 0.36; volumetric features begin to resolve. **e, f**) Result and histogram for NA = 0.72; the geometry is reproduced with high fidelity. Note that the physical field of view scales inversely with NA.

NA = 0.72 (pixel size 0.28 μm). In all cases, we optimize a sequence of 30 time-multiplexed phase patterns.

The results are summarized in Figure 15. At NA = 0.12 (Figure 15a), the reconstruction is severely degraded. The limited angular diversity results in a large missing cone in the frequency domain, causing elongation of features along the optical axis and preventing the successful resolution of the boat's hull and cabin.

Increasing the NA to 0.36 (Figure 15c) significantly improves axial confinement, with the boat geometry becoming clearly recognizable. At NA = 0.72 (Figure 15e), the system achieves true volumetric addressing; the complex overhangs and internal voids of the #3DBenchy are almost fully reproduced. This improvement

is quantitatively confirmed by the dose histograms (Figure 15b, d, f), which show a progressive sharpening of the contrast between object and void regions as NA increases.

These results indicate that SHVAM is capable of high-fidelity volumetric printing given sufficient optical access. While we simulated up to NA = 0.72, immersion objectives could theoretically extend effective NAs to  $\approx 1.4$ , further minimizing the missing cone. We note that achieving this resolution experimentally would require accounting for chemical effects (as we presented in this work); as diffusion would blur these fine features, such high-NA implementations would likely necessitate diffusion-engineered resins or reduced print times.